Mechanism and Machine Theory 153 (2020) 104021

Contents lists available at ScienceDirect

Mechanism and Machine Theory

journal homepage: www.elsevier.com/locate/mechmachtheory

Stiffness modeling of a variable stiffness compliant link☆

Tyler Morrison*, Hai-Jun Su

Department of Mechanical and Aerospace Engineering, The Ohio State University, 201 W. 19th Avenue, Columbus, OH 43210, USA

ARTICLE INFO

Article history:
Received 22 April 2020
Revised 12 June 2020
Accepted 1 July 2020
Available online xxx

Keywords:
Variable stiffness
Compliant mechanisms
Mechanics modeling
Compliance matrix
Screw theory

ABSTRACT

Recently, a variable stiffness robotic link based on the rotating beam concept has been developed for applications in physical human robot interaction. A substantial challenge for design of such links is the modeling of stiffness behavior to permit stiffness control. In this paper we present a general 3D model of the link stiffness using screw theory and compliance matrices as well as a planar model for the lateral and torsional stiffness. Since axial buckling is a major failure mode, we also derive an analytical model for predicting axial buckling behavior. The analytical models are compared to the finite element method and experimental results. One of the challenges involved in design and analysis of variable stiffness links is the parasitic compliance of the mechanical elements that support and drive the active portion of the mechanism. For the design analyzed in this paper, we use the models we derive to identify the major sources of parasitic compliance and suggest optimizations to minimize their effects. These results can be used as guidelines for designing variable stiffness links.

1. Introduction

Variable stiffness links (VSLs) such as [1–3,5–7] have been proposed for use in collaborative robots or corobots for safer human-robot-interaction [8–11], and have many other potential uses such as in prosthetics and medical devices [12]. Just as models of gear loads or pipe flow allow engineers to design those components more easily, the design of a VSL can be significantly aided by the development of a simple yet descriptive model of its stiffness-changing behavior. Furthermore, a model of how the device stiffness changes as a function of the control variable is a prerequisite for general impedance control of a robot constructed from VSLs. Accordingly, it is valuable to be able to obtain an analytical model of VSL stiffness as a function of the control variable.

Some VSLs can be modeled using techniques from compliant mechanisms, for which researchers have proposed a number of methods. The psuedo-rigid-body model (PRBM) effectively lumps the distributed compliance of the mechanism into a series of discrete compliant elements [13,14]. The parameters of this model are determined by optimization offline and depend on loading and boundary conditions. An interesting extension of this method involves lumping the mass distribution of the mechanism as well as the compliance to allow for efficient modeling of compliant mechanism dynamics [15]. This is particularly useful for modeling impacts. The beam constraint model (BCM) alleviates the need for offline optimization and improves modeling of the elastokinematic effect at the cost of increased mathematical complexity [16]. The chained

☆ This material is based upon work supported by the National Science Foundation under Grant No: CMMI-1637656. Any opinions, findings, and conclusions or recommendations expressed in this material are those of the authors and do not necessarily reflect the views of the funding agencies.

* Corresponding author.
E-mail addresses: morrison.730@osu.edu (T. Morrison), su.298@osu.edu (H.-J. Su).

https://doi.org/10.1016/j.mechmachtheory.2020.104021
0094-114X/

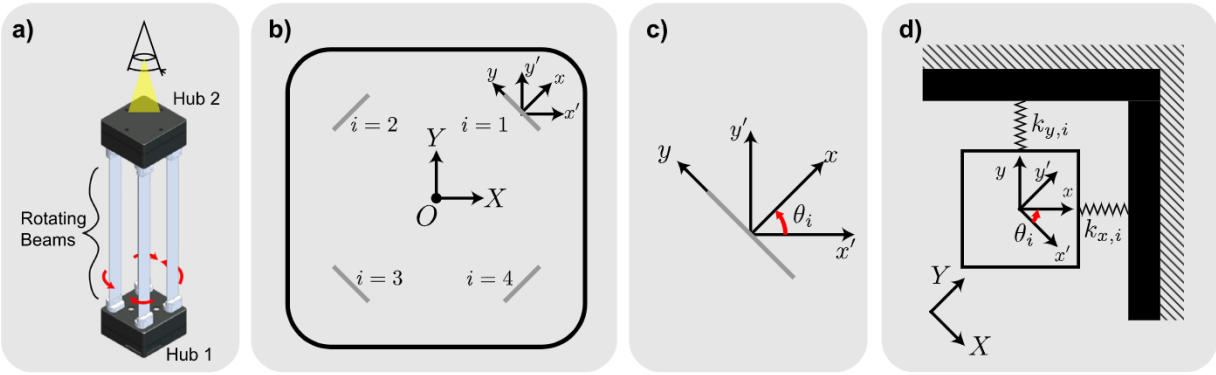

Fig. 1. The planar model for lateral stiffness. a) Top down view of the cross-section. b) The cross-section shown with the relevant reference coordinate frames. c) The coordinate frame of one beam. d) The orthogonal stiffness model used for each beam in the rotating reference frame.

BCM (CBCM) extends the BCM formulation for use with larger deformations by breaking the beam flexure up into a small number of shorter beams and applying the BCM to each of them [17,18]. These methods provide a basis for the analysis of flexures subjected to large deflections but are usually limited to the planar case, however, there has been some effort to extend the CBCM to spatial mechanisms [19], and the PRBM to 3D deformations [20].

The stiffness of spatial mechanisms can be efficiently analyzed through the use of screw-theory based compliance and stiffness matrices [21,22]. Such an approach has been used in the past for compliant serial robots such as [23]. This method only requires matrix algebra to compute and can be expressed analytically for most mechanisms, but is usually limited to linearly approximating the stiffness associated with small deflections. However, in [24], the authors demonstrate the use of screw-theory combined with non-linear modeling in their constraint-force-based (CBM) method for analysis of a complex compliant mechanism constructed from wire elements.

In practice, the stiffness of VSLs has been modeled by a variety of ad-hoc methods. In [1], the stiffness model is constructed by modeling the cross-section geometry shape-morphing behavior and using the area moment of inertia to construct a PRBM. In [5], the stiffness model is constructed by solving the beam equations and adding corrections to approximate the parasitic compliance of the rest of the structure. In both these works, correction terms were required to accurately account for the compliance of ancillary parts of the structure apart from the beam flexure. The common result from these studies is that when the VSL is in its higher stiffness mode, the compliance of the other passive components in series with the active component begin to have substantial influence on the design stiffness. We refer to this as the "parasitic compliance" effect. Comparison of these prior works suggests that a model of variable stiffness behavior for a VSL cannot be accurate over a wide range of stiffness without accounting for parasitic compliance.

In this paper we analyze the mechanics of the novel rotating beam link (RBL) VSL introduced in our recent work [7]. The link, shown in Fig. 1a), is designed to vary its stiffness as a function of a single input parameter – in this case, the angle of rotation of each of the four individual beams about their central axes. Both hubs of the link include a small servomotor connected to a series of gears that synchronize the rotations of the beams. The two servomotors are calibrated and synchronized to ensure that the beams are held at the same angle at both ends. More information on the design of the link can be found in our previous work [7].

1.1. Motivation

One of the main motivations for the design of VSLs is that they may be implemented in serial robotic manipulators to improve the safety of physical human-robot-interaction (pHRI). Consider that the impedance of a serial link robot with variable stiffness actuators (VSAs) can be planned along its kinematic trajectory [25,26]. Extending this concept to VSLs, and defining the impedance trajectory based on a method for estimating and minimizing the risk of injury to a human during a hypothetical impact [4,27], may allow for the planning of combined kinematic and impedance trajectories that minimize the severity of a collision for the robot and its surroundings [28,29]. Detecting [30] or predicting [31] collisions and changing stiffness reactively may also be possible for a sufficiently fast-acting VSL. Of course, informative models of a VSL design's behavior are a prerequisite for these applications.

Effectively exploiting the additional functionality of a VSL compared to a conventional fixed-stiffness link requires both a high stiffness when positional accuracy or high-bandwidth actuation is required, and low stiffness when impact safety is more critical or during contact with the environment. It follows that a useful VSL should have a sufficiently large stiffness ratio. In addition, the time it takes to change stiffness, the mass of the device, and its complexity should be minimized. For an overview and comparison of techniques for changing structural stiffness, the authors recommend [32] and [12]. Here we will briefly review some existing VSL designs.

A VSL based on morphing the link cross-section was introduced in [33]. The lateral stiffness of this design achieves a stiffness ratio of 3.6. In [2], the authors vary the stiffness of a link by pneumatically pressurizing its structure. Their results show a lateral stiffness ratio somewhere in the range of 1.5 to 2. Authors in [3] and [5] developed VSL solutions based on varying the effective length of parallel guided beams, which achieved relatively high stiffness ratios of approximately 20 and 10 respectively. The electrostatic layer-jamming concept in [6] achieves a maximum stiffness ratio of approximately 7, albeit the authors measure it differently than others. In a direct comparison, it is likely nearer to 3. While these top-line numbers can give a rough comparison of the designs, each of these designs has a different length, cross-section, mass, and stiffness range (rather than the ratio). Accordingly, a more in-depth comparison between them would be required to make a decision on which design to use for a particular application. To that end, they may each be optimal for different applications.

1.2. Overview

In the following sections, first, we will investigate analytical modeling of the design that accounts for the parasitic compliance effect. We will outline one approach for stiffness derivation by using assumptions about constraints and then deriving the stiffness of the beams from first principles. Additionally, because buckling is a concern for most uses of the device, we develop a model of axial buckling. Next, we present a finite element model for comprehensive simulation of the prototype which bridges gaps in our analytical approach. Finally, we will present results from extensive experimental testing on the design regarding lateral stiffness, torsional stiffness and axial buckling.

2. Planar model of stiffness

The rotating beam link (RBL) concept studied in this article consists of four long slender beams as illustrated in Fig. 1a). Each beam is actuated to rotate about its own central axis. Their rotation is synchronized to maintain reflective symmetry across each of the principal axes of the cross-section. As a result, at its core, the RBL is a spatial compliant mechanism.

However, the three degrees of freedom of Hub 2 relative to Hub 1 in the $X-Y$ plane (two translation, one rotation) are of primary interest. The two translation degrees of freedom correspond to lateral loads on the link such as impacts or payloads. The rotation degree of freedom corresponds to torsional loads around the central Z axis of the link such as impacts or payloads on links farther down the chain of the serial robot. Because these degrees of freedom can be modeled using a planar derivation, we refer to these as "planar models."

2.1. Planar lateral stiffness derivation

Our first goal is to derive an analytical model of lateral stiffness as a function of the changing beam angles. Lateral stiffness is of primary interest because of the role it plays in determining impact dynamics [8,11] and deflection under load. For the link in this study, the lateral direction will usually lie in the $X-Y$ plane. However, for simplicity, we assume that the X axis is the lateral direction of interest. Fig. 1(b-d) illustrates the reference frames used for this derivation, and indicates the two stiffness components that describe our assumed lateral-stiffness model of each beam: $k_{x,i}$ and $k_{y,i}$.

First, assume that each beam indexed by i has a diagonal stiffness matrix in its rotating $x-y$ frame

$$\left[K_{xy,i}\right] = \begin{bmatrix} k_{x,i} & 0 \\ 0 & k_{y,i} \end{bmatrix} \quad \text{where } i = 1, \ldots, 4. \tag{1}$$

The individual components $k_{x,i}$ and $k_{y,i}$ represent the lateral stiffness associated with a transverse tip-deflection of the beam in the direction of the short and long sides of its cross-section respectively.

Next, assume that the transformation between the frame $x'-y'$ and $x-y$ is given by the rotation angle θ_i and the 2D rotation matrix

$$[R(\theta_i)] = \begin{bmatrix} \cos\theta_i & -\sin\theta_i \\ \sin\theta_i & \cos\theta_i \end{bmatrix}. \tag{2}$$

Then, defining

$$\mathbf{F}_{x'y',i} = \begin{bmatrix} F_{x',i} \\ F_{y',i} \end{bmatrix} \text{ and } \boldsymbol{\delta}_{x'y'} = \begin{bmatrix} \delta_{x'} \\ \delta_{y'} \end{bmatrix}, \tag{3}$$

it follows that

$$\mathbf{F}_{x'y',i} = [R(\theta_i)]\left[K_{xy,i}\right][R(\theta_i)]^{\mathsf{T}}\boldsymbol{\delta}_{x'y'}. \tag{4}$$

Here, $F_{x',i}$ and $F_{y',i}$ are the force components applied to the ith beam, θ_i is the beam rotation angle, and $\delta_{x'}$ and $\delta_{y'}$ are the deflection components, which are equivalent for all beams given they are fixed to the same rigid body.

Therefore, the stiffness matrix of the link for planar lateral forces can be written:

$$\left[K_{x'y',i}\right] = [R(\theta_i)]\left[K_{xy,i}\right][R(\theta_i)]^{\intercal} = \begin{bmatrix} \frac{k_{x,i}+k_{y,i}}{2} + \frac{k_{x,i}-k_{y,i}}{2}\cos(2\theta_i) & \left(k_{x,i}-k_{y,i}\right)\sin(2\theta_i) \\ \left(k_{x,i}-k_{y,i}\right)\sin(2\theta_i) & \frac{k_{x,i}+k_{y,i}}{2} + \frac{k_{y,i}-k_{x,i}}{2}\cos(2\theta_i) \end{bmatrix}. \tag{5}$$

Our first observation about this result is that all components are periodic on the interval π. This is due to the fact that the beams themselves have rotational symmetry with period π. The second observation about this matrix is that the components have the same structure as the equations for rotating the reference coordinate system of a second moment of inertia [34]. This follows from the fact that the stiffness for a deflection that does not lie along its principal axes can still be computed from 1D classical beam theory, however, the second moment of inertia must be computed by rotating its axis to align with the axis of bending.

So far, we have determined the stiffness matrix of one of the four individual beams that makes up the main structure of the link. To determine the stiffness of the entire link we have to sum the stiffness matrices for each of the four beams. This follows from the fact that the beams are assembled in parallel which one another. However, because the rotations of the beams in this design are synchronized to ensure mirror symmetry across both the X and Y axes, two of the beams have a rotation angle $-\theta_i$ – in the opposite direction. Numbering according to the quadrant the beam is in, in the $X-Y$ frame, we let $\theta_1 = \theta$, $\theta_2 = -\theta$, $\theta_3 = \theta$, and $\theta_4 = -\theta$. As a result, the stiffness of the entire link can be written:

$$[K_{XY}] = \sum_{i=1}^{4}\left[K_{x'y',i}(\theta_i)\right]. \tag{6}$$

The result of computing this sum is the following matrix:

$$[K_{XY}] = \begin{bmatrix} \frac{\sum k_{x,i}+\sum k_{y,i}}{2} + \frac{\sum k_{x,i}-\sum k_{y,i}}{2}\cos(2\theta) & \left(k_{x,13}+k_{y,24}-k_{y,13}-k_{x,24}\right)\sin(2\theta) \\ \left(k_{x,13}+k_{y,24}-k_{y,13}-k_{x,24}\right)\sin(2\theta) & \frac{\sum k_{x,i}+\sum k_{y,i}}{2} + \frac{\sum k_{y,i}-\sum k_{x,i}}{2}\cos(2\theta) \end{bmatrix} \tag{7}$$

where for clarity we have denoted $k_{x,ij} = k_{x,i} + k_{x,j}$ and $k_{y,ij} = k_{y,i} + k_{y,j}$.

We can make a few more observations of the behavior of the link based on the structure of this matrix. First, its sinusoidal components retain the same period as its constituent matrices. Second, in the case that $k_{x,13} + k_{y,24} - k_{y,13} - k_{x,24} = 0$, the matrix loses its off-diagonal coupling terms and becomes a 2D diagonal stiffness matrix. This condition occurs if $k_{x,i}$ are equal and all $k_{y,i}$ are equal. This fact arises because the $\sin(2\theta)$ terms of the $i=1$ and $i=3$ matrices cancel out the $\sin(-2\theta)$ terms from the $i=2$ and $i=4$ matrices. In other words, one insight that we can gain from this model is that the choice of reflection-symmetric cross-section results in a simplified, diagonal, stiffness matrix.

However, one limitation discovered during testing is that application of a pure lateral load results in buckling of some of the beams. The buckling that occurs in this load configuration is due to a combination of the elastic instability resulting from a transverse force across a beam with a high aspect ratio, a moment applied across a beam with a high aspect ratio, and the high internal axial compressive force resulting from bending across the original (pre-buckling) neutral axis. Fig. 2 gives an illustration of the buckling behavior during lateral displacement in the direction of the X axis. In Fig. 2b) the unloaded link has relatively straight beams. After the load is applied in the $+X$ direction, the two beams on the $+X$ side of the link bow outward indicating a buckling mode with a wavelength approximately equal to the length of the beam. Fig. 2c) shows how this behavior results in a rotation of Hub 2 and a departure from fixed-guided end conditions.

As a result of this buckling behavior, $k_{x,i}$ and $k_{y,i}$ need to be determined on a case by case basis. This process requires special considerations that will be described later in Section 2.3 and Section 2.4.

2.2. Planar torsional stiffness derivation

The torsional stiffness of the link may be relevant to forces during impacts or the load-carrying capacity of a multi-link robot in some situations. Therefore, modeling the RBL's torsional stiffness is of significant interest as well. The torsional stiffness is defined to be the rate of change of the moment M_Z applied to the distal hub (Hub 2) relative to the angular displacement ϕ_Z of Hub 2 relative to Hub 1.

The hubs are orders of magnitude stiffer than the beam components as a result of their geometry; consequently, we assume that the hubs are effectively rigid bodies. Therefore, the four beams carry the load in parallel and the deflections at the tip of each beam are equivalent. Accordingly, for a small twist of Hub 2 relative to Hub 1 about the Z axis denoted ϕ_Z in Fig. 3, each beam has an equivalent twist angle $\phi_z = \phi_Z$ (the lower case z indicates that the rotation occurs around the beam-centered frame) in addition to a small linear deflection $\boldsymbol{d}$ resulting from the twist. The central z axes of the beams have a displacement $\boldsymbol{r}$ from the central Z axis of the link. The small deflection at the beam $\boldsymbol{d}$ is perpendicular to $\boldsymbol{r}$ on account of the fact that it is the tangent to the arc traced out when the center of the beam rotates about Z.

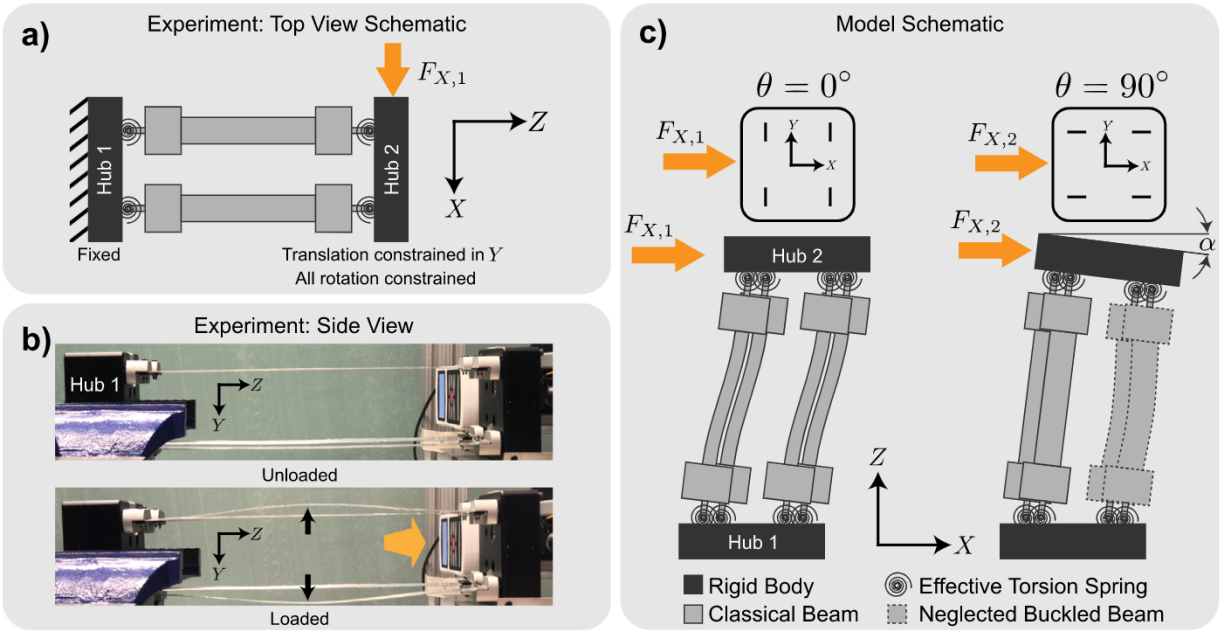

Fig. 2. When subjected to a lateral load in the $+X$ direction, the beams on the $+X$ side of the link buckle outward while the beams on the $-X$ side do not. a) The top-view schematic of the link during a lateral load experiment using a depiction of the beam as it is modeled throughout the paper: consisting of shafts and blocks at either end of a central beam sheet, and with equivalent torsion springs on each end that rotate along with the beams and account for the incidental rotational compliance where the shafts are mounted into their bearings in the hub. b) Experimental observations of the buckling effect in photos before and during lateral loading. c) We illustrate that this process occurs only as the beam rotation angle causes the link to stiffen and the lateral load is aligned with the longer side of the beam sheets. The lateral buckling results in a rotation of the hub tip, α, and approximately cantilever boundary conditions for the remaining unbuckled beams.

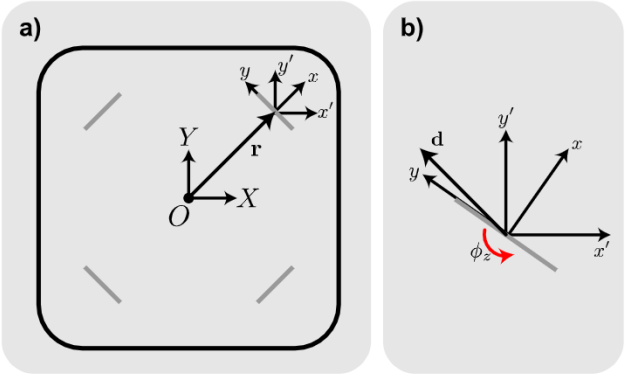

Fig. 3. Coordinate frames and vectors for the planar torsional stiffness model. a) The link cross-section. b) An individual beam.

We can express both the moment-arm $\boldsymbol{r}$ and the small displacement $\boldsymbol{d}$ for each beam as:

$$\mathbf{r}_i = r\begin{bmatrix}\cos\left(\frac{\pi}{2}i - \frac{\pi}{4}\right)\\ \sin\left(\frac{\pi}{2}i - \frac{\pi}{4}\right)\end{bmatrix} \tag{8}$$

and

$$\mathbf{d}_i = r\phi_Z\begin{bmatrix}\cos\left(\frac{\pi}{2}i + \frac{\pi}{4}\right)\\ \sin\left(\frac{\pi}{2}i + \frac{\pi}{4}\right)\end{bmatrix} \tag{9}$$

where the scalar r is the diagonal distance from the center of the link to the center of the beams.

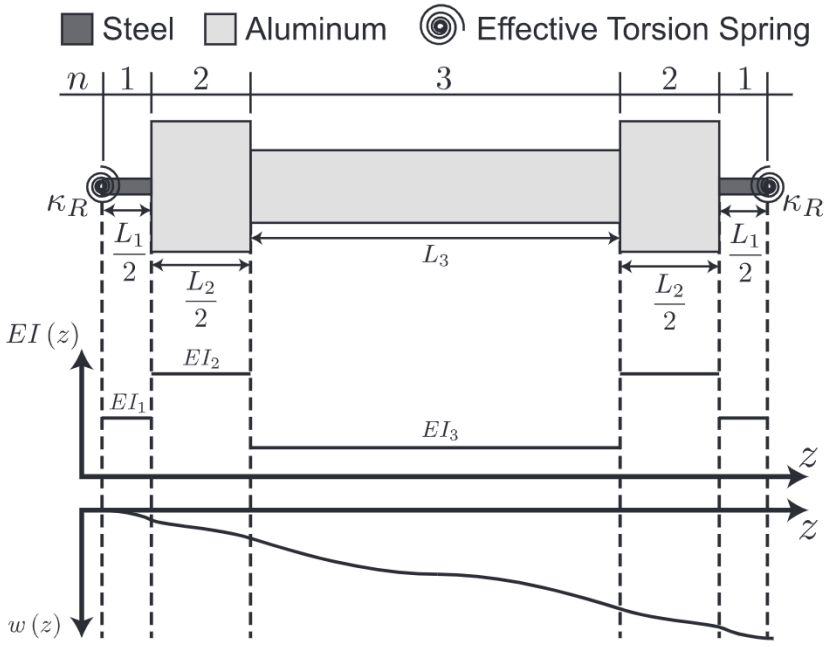

Fig. 4. Illustration of the model used to derive the stiffness of each beam. The beam can be divided into five sections with three sets of material and cross-section properties for $n = 1, 2, 3$. In addition, effective torsion springs on either end represent the slight bearing compliance.

Now, we can express the total reaction moment as the sum across all beams:

$$M_Z = \sum_{i=1}^{4} \left(\kappa_{z,i}\phi_Z + \mathbf{e}_3^{\intercal} \left(\mathbf{r}_i \times [R(\theta_i)] \left[K_{xy,i} \right] [R(\theta_i)]^{\intercal} \mathbf{d}_i \right) \right) \tag{10}$$

where κ_z is the torsional stiffness of each beam and $\boldsymbol{e}_3$ is the $+Z$ unit vector $[0, 0, 1]^{\intercal}$. In this case, $[R(\theta_i)]$ is the 3D rotation matrix about z:

$$[R(\theta_i)] = \begin{bmatrix} \cos\theta_i & -\sin\theta_i & 0 \\ \sin\theta_i & \cos\theta_i & 0 \\ 0 & 0 & 1 \end{bmatrix}. \tag{11}$$

The result is the equation for the reaction torque:

$$M_Z = \sum_{i=1}^{4} \left(\kappa_{z,i} + r^2 \left(\frac{k_{x,i} + k_{y,i}}{2} + \frac{k_{y,i} - k_{x,i}}{2} \sin(2\theta) \right) \right) \phi_Z \tag{12}$$

and the overall link torsional stiffness:

$$\kappa_Z = \frac{dM_Z}{d\phi_Z} = \sum_{i=1}^{4} \left(\kappa_{z,i} + r^2 \left(\frac{k_{x,i} + k_{y,i}}{2} + \frac{k_{y,i} - k_{x,i}}{2} \sin(2\theta) \right) \right). \tag{13}$$

Just as in Eq. (7) in the previous section, $k_{x,i}$, $k_{y,i}$, and $\kappa_{z,i}$ remain unknown and will be defined next in Section 2.3.

2.3. Determining the beam stiffness components k_x, k_y, κ_z

Up to this point, we have been using k_x, k_y, and κ_z as stand-ins for the lateral-x, lateral-y, and torsional stiffness of a beam. In this section, we will derive their values by applying classical beam theory to the piecewise model of the beam shown in Fig. 4.

Specifically, for k_x and k_y, we assume that the flexural rigidity, EI is a piecewise function of z, the axis along the length of the beam. The torsion springs κ_R are included by assuming they define a linear relationship between the local bending moment and the local beam slope $w'(z)$.

Consider a lateral load in the $+X$ direction of the link as shown in Fig. 2. In order to match observed behavior of the prototype to the theory, we need to consider two sets of boundary conditions. In the first case, all four beams share the applied load equally and have equal deflection. The distal hub (Hub 2) does not rotate around the Y axis. As a result, the

beam tips translate in the $+X$ direction with fixed-guided boundary conditions (FG). In the second case, the two beams on the $+X$ half of the beam experience compressive forces with high leverage relative to the lateral force. As a result, they buckle and their stiffness decreases dramatically, so much so that it can be considered negligible compared to the stiffness of the remaining unbuckled beams. In this case, the distal hub (Hub 2) does undergo rotation around the Y axis. We consider the boundary conditions for the remaining two unbuckled beams to be cantilever (CL).

Considering the case of a beam with a force at the tip under fixed-guided boundary conditions, and applying classical Euler-Bernoulli beam theory yields:

$$k_{FG}^{-1} = \left(\frac{2\kappa_R}{(L_1+L_2+L_3)^2}\right)^{-1} + \left(\frac{12E_3I_3}{L_3^3}\right)^{-1} + \left(\frac{12E_2I_2}{(L_2+L_3)^3}\right)^{-1} - \left(\frac{12E_2I_2}{L_3^3}\right)^{-1} + \left(\frac{12E_1I_1}{(L_1+L_2+L_3)^3}\right)^{-1} - \left(\frac{12E_1I_1}{(L_2+L_3)^3}\right)^{-1} \tag{14}$$

Considering the case of a beam a force at the tip under cantilever boundary conditions, and applying classical Euler-Bernoulli beam theory yields:

$$k_{CL}^{-1} = \left(\frac{\kappa_R}{(L_1+L_2+L_3)^2}\right)^{-1} + \left(\frac{12E_1I_1}{L_1(4L_1^2+9L_1(L_2+L_3)+6(L_2+L_3)^2)}\right)^{-1} + \left(\frac{12E_2I_2}{L_2(3L_1^2+4L_2^2+9L_2L_3+6L_3^2+6L_1(L_2+L_3))}\right)^{-1} + \left(\frac{12E_3I_3}{L_3(4L_3^2+3(L_1+L_2)(L_1+L_2+2L_3))}\right)^{-1} \tag{15}$$

Here, κ_R is the equivalent torsion spring stiffness, E_n is the elastic modulus I_n is the second moment of area, L_n is the length, and n is the index corresponding to sections of the beam as indicated in Fig. 4.

Notably, Eq. (14) has a simple sum of components structure as a result of the symmetry of cantilever boundary conditions. Eq. (15), on the other hand, cannot be simplified and broken down similarly.

The torsional stiffness of a beam, κ_z can be determined with less effort. Consider each component of the beam as a torsion spring. The five components (the equivalent torsion springs do not have any compliance for torsion around the z axis) are in series and therefore their equivalent stiffness can be determined by the inverse of the sum of inverses – or more appropriately, their compliance is simply the sum of components:

$$\kappa_z^{-1} = \sum_{n=1}^{3}\left(\frac{G_nJ_n}{L_n}\right)^{-1}. \tag{16}$$

Where G_n is the shear modulus, J_n is the torsional stiffness constant, L_n is the length, and n is the index indicating the beam segment. For the circular cross-section of the shafts, the torsional stiffness constant is equivalent to the polar moment of inertia for circular cross-sections:

$$J_1 = \frac{\pi}{32}d_1^4. \tag{17}$$

For the rectangular cross-section of the beams ($n = 3$) and blocks ($n = 2$):

$$J_n = a_nb_n^3\left(\frac{16}{3} - 3.36\frac{b_n}{a_n}\left(1 - \frac{b_n^4}{12a_n^4}\right)\right) \text{ for } a_n \geq b_n,\ n = 2 \text{ or } 3;\ \text{where } 2a_3 = w_3,\ 2b_3 = t_3;\ 2a_2 = w_2,\ 2b_2 = w_2, \tag{18}$$

based on the relation in [35].

2.4. Analytical equations for lateral and torsional stiffness

Finally, let us combine the results from the previous three sections to develop analytical models of the lateral and torsional stiffness of the RBL in question as functions of the rotating link beam angle, θ.

First, we reference Eqs. (7), (14), and (15) to define the lateral stiffness for the link while subjected to a load in the $+X$ direction applied to the tip of the RBL. Let $I_{y,n}$ be the second moment of area of the nth section of the beam taken about the y axis of the beam. Let $I_{x,n}$ be the same for the x axis.

Now, let

$$k_{x,FG} = k_{FG} \text{ with } I_n = I_{y,n} \quad \text{for} \quad n = 1, 2, 3, \tag{19}$$

$$k_{y,FG} = k_{FG} \text{ with } I_n = I_{x,n} \quad \text{for} \quad n = 1, 2, 3, \tag{20}$$

$$k_{y,CL} = k_{CL} \text{ with } I_n = I_{x,n} \quad \text{for} \quad n = 1, 2, 3, \tag{21}$$

define the stiffness of a beam in each direction under either fixed guided (FG) or cantilever (CL) boundary conditions.

When the beams are in their compliant direction relative to the X axis, that is, when $\theta = 0$, no buckling occurs under lateral loading. That is, we consider

$$k_{x,i} = k_{x,FG} \quad \forall i. \tag{22}$$

When the beams are in their stiffest direction relative to the X axis, that is, when $\theta = \pi/2$, the two beams on the $+X$ side of the link buckle and can be assumed to contribute no support. As a result, we assume the two beams on the $-X$ side of the link support the entire load themselves but under cantilever boundary conditions. That is we consider,

$$k_{y,1} = 0, \quad k_{y,4} = 0, \tag{23}$$

and

$$k_{y,2} = k_{y,CL}, \quad k_{y,4} = k_{y,CL}. \tag{24}$$

Substituting these values into Eq. (7) gives the model for lateral stiffness of the RBL first reported in [7] as:

$$k_X(\theta) = \frac{dF_X}{d\delta_X} = (2k_{x,FG} + k_{y,CL}) + (2k_{x,FG} - k_{y,CL})\cos(2\theta). \tag{25}$$

Second, we define a model of the torsional stiffness of the link while subjected to a moment about the central Z axis of the link. The buckling effect that it is necessary to account for in the lateral stiffness model is not present during torsion. As a result, for torsional stiffness, we set

$$k_{x,i} = k_{x,FG}, \quad k_{y,i} = k_{y,FG}, \quad k_{z,i} = \kappa_z \quad \forall i. \tag{26}$$

Substituting Eq. (26) into Eq. (13) gives the model for torsional stiffness of the RBL as:

$$\kappa_Z(\theta) = \frac{dM_Z}{d\phi_Z} = 4\kappa_z + 2r^2\Big(\big(k_{x,FG} + k_{y,FG}\big) - \big(k_{x,FG} - k_{y,FG}\big)\sin(2\theta)\Big). \tag{27}$$

3. Screw-theory for spatial stiffness matrices

3.1. Review of screw theory and compliance matrices

In the previous section, we derived two main results: Eq. (25) for the lateral stiffness of the link for a deflection in the positive X direction and Eq. (27) for the torsional stiffness of the link for a rotational displacement in the Z axis (positive or negative). However, in order to obtain theses results, we had to solve a series of five loosely coupled fourth order differential equations with a total of six sets of boundary conditions between them.

The screw-theory derivation method can help us avoid this step and provide a stiffness matrix that is 6×6, i.e.: one that includes all six degrees of freedom [21,22].

A twist, a vector quantity expressing a generalized deflection in a specific frame, can be written:

$$\mathbf{T} = [\phi_x,\ \phi_y,\ \phi_z,\ \delta_x,\ \delta_y,\ \delta_z]^\intercal \tag{28}$$

where ϕ_x, ϕ_y, and ϕ_z are the angular deflections in the reference frame, and δ_x, δ_y, and δ_z are the linear deflections in the reference frame.

A wrench, a vector quantity expressing generalized force in a specific frame, can also be written:

$$\mathbf{W} = [F_x,\ F_y,\ F_z,\ M_x,\ M_y,\ M_z]^\intercal \tag{29}$$

where F_x, F_y, and F_z are forces in the reference frame and M_x, M_y, and M_z are moments in the reference frame.

Accordingly, a stiffness matrix $[K]$ transforms an input twist into the reaction wrench, and a compliance matrix $[C]$ transforms an input wrench into the corresponding deflection such that $[K]$ and $[C]$ are inverses. In summary:

$$\mathbf{W} = [K]\mathbf{T}, \quad \mathbf{T} = [C]\mathbf{W}, \quad [C] = [K]^{-1}. \tag{30}$$

Note that under this definition, compliance and stiffness matrices are not diagonally symmetric due to the definitions of deformation twists and load wrenches.

The coordinate transformation of a compliance or stiffness matrix from one reference frame to the other is conducted via the so-called adjoint matrix $[Ad]$ written as

$$[Ad] = \begin{bmatrix} R & 0 \\ DR & R \end{bmatrix}. \tag{31}$$

The matrix $[R] \in SO(3)$ is the 3×3 rotation matrix and $[D]$ is the skew-symmetric matrix for the translation vector $\mathbf{d} = (d_1, d_2, d_3)^\intercal$,

$$[D] = \begin{bmatrix} 0 & -d_3 & d_2 \\ d_3 & 0 & -d_1 \\ -d_2 & d_1 & 0 \end{bmatrix}. \tag{32}$$

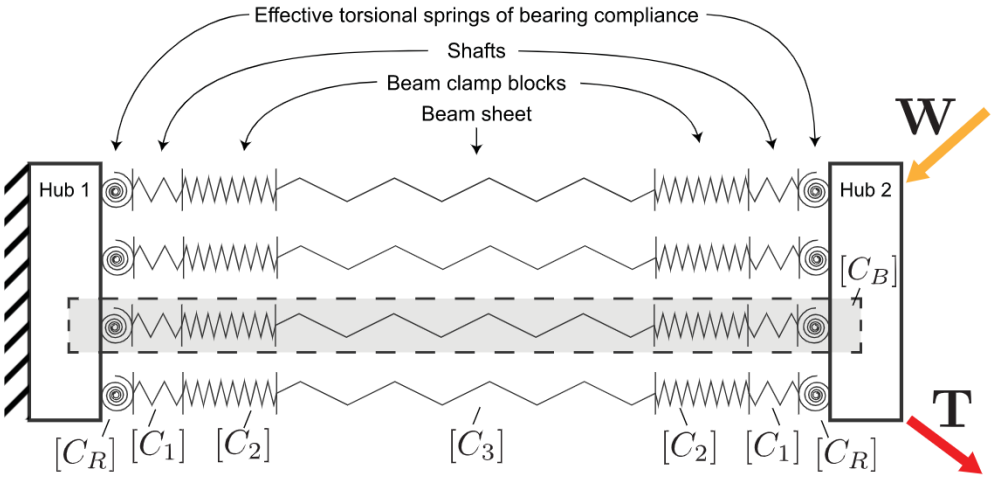

Fig. 5. A schematic of the rotating beam link indicating the topology of the design as assumed in the derivation of the compliance matrices for a wrench $\boldsymbol{W}$ and resulting twist $\boldsymbol{T}$ in the frame of Hub 2. The compliance matrices of each individual component can be combined to get the compliance matrix for a beam: $[C_B]$.

For convenience, let us define the coordinate transformation operator, $\boldsymbol{Tr}$, on a stiffness or compliance matrix $[X]$ as

$$\left[X'\right] = \boldsymbol{Tr}(X, R, \mathbf{d}) = [Ad][X][Ad]^{-1}. \tag{33}$$

For serially connected mechanisms – in which each element has the same applied load when written in the same reference frame – the compliance matrix of the whole is the sum of the compliance matrices of the parts. Predictably, for parallel mechanisms – in which each element has the same deflection when expressed in the same reference frame – the stiffness matrix of the whole is the sum of the stiffness matrices of the parts. See [22] for more details on algebra and operations of compliance and stiffness matrices.

In the following sections, we will apply these operations and algebra to derive the equivalent compliance/stiffness of a general RBL.

3.2. Compliance matrix derivation

To derive the compliance matrix of the rotating beam link, we assume that the RBL has the topology shown in Fig. 5. In this topology, the four identical rotating beams are connected in parallel between the two hubs. Each beam is a serial chain consisting of two effective torsion springs, two shafts, two beam clamp blocks and a beam sheet that all rotate together about their central axis by θ. To develop an accurate model, we must consider the contribution of compliance of all these components to the final compliance matrix of the entire RBL.

In order to obtain the compliance matrix for the entire RBL, first we derive the compliance matrix of a single beam according to a local reference frame placed at its tip. Then we express the stiffness matrix of each beam in a reference frame at the center of the tip of the RBL, and sum them to obtain the total stiffness matrix which is inverted to obtain the compliance matrix.

For a reference frame at the tip of an extruded solid with a constant cross-section and indexed by $n = 1, 2, 3$, the compliance matrix is written:

$$[C_n] = \begin{bmatrix} 0 & \frac{-L_n^2}{2E_nI_{x,n}} & 0 & \frac{L_n}{E_nI_{x,n}} & 0 & 0 \\ \frac{L_n^2}{2E_nI_{y,n}} & 0 & 0 & 0 & \frac{L_n}{E_nI_{y,n}} & 0 \\ 0 & 0 & 0 & 0 & 0 & \frac{L_n}{G_nJ_n} \\ \frac{L_n^3}{3E_nI_{y,n}} & 0 & 0 & 0 & \frac{L_n^2}{2E_nI_{y,n}} & 0 \\ 0 & \frac{L_n^3}{3E_nI_{x,n}} & 0 & \frac{-L_n^2}{2E_nI_{x,n}} & 0 & 0 \\ 0 & 0 & \frac{L_n}{A_nE_n} & 0 & 0 & 0 \end{bmatrix} \tag{34}$$

Table 1
Compliance matrices of individual components and their corresponding coordinate transformation for each serial chain.

i	Compliance Matrix $\left[C_i'\right]$	Translation $\boldsymbol{t}_i$	Rotation $[R_i]$
1	$[C_R]$	$-(L_1+L_2+L_3)\boldsymbol{k}$	$[I]$
2	$[C_1]$	$-(L_1/2+L_2+L_3)\boldsymbol{k}$	$[I]$
3	$[C_2]$	$-(L_1/2+L_2/2+L_3)\boldsymbol{k}$	$[I]$
4	$[C_3]$	$-(L_1/2+L_2/2)\boldsymbol{k}$	$[I]$
5	$[C_2]$	$-(L_1/2)\boldsymbol{k}$	$[I]$
6	$[C_1]$	$\boldsymbol{0}$	$[I]$
7	$[C_R]$	$\boldsymbol{0}$	$[I]$

where L_n is the length, A_n is the cross-sectional area, $I_{x,n}$ and $I_{y,n}$ are the second moments of area, J_n is the torsional stiffness constant, E_n is the elastic modulus, and G_n is the modulus of rigidity. Therefore, the shafts, blocks and sheets shown in Fig. 4 can each be approximated with their own compliance matrices $[C_1]$, $[C_2]$, and $[C_3]$.

The beams are fixed to each hub with a certain amount of compliance due to give in the mounting components such as the ball bearings. The flexibility in the root of each beam can be approximately modeled as two orthogonal equivalent torsion springs and the compliance matrix:

$$[C_R] = \begin{bmatrix} 0 & 0 & 0 & \frac{1}{\kappa_R} & 0 & 0 \\ 0 & 0 & 0 & 0 & \frac{1}{\kappa_R} & 0 \\ 0 & 0 & 0 & 0 & 0 & 0 \\ 0 & 0 & 0 & 0 & 0 & 0 \\ 0 & 0 & 0 & 0 & 0 & 0 \\ 0 & 0 & 0 & 0 & 0 & 0 \end{bmatrix}. \tag{35}$$

Here we neglected the compliance in all directions (i.e. making them ideally rigid) except for rotation due to moments about the X and Y axes. Essentially, we model the joint as a universal joint with torsion springs on each hinge, each with the torsional spring rate κ_R. The value of κ_R was determined by experimentally measuring the rotational stiffness of each bearing in several directions and computing the mean.

We combine the seven components that make up a beam modeled as shown in Figs. 4 and 5 to obtain the total compliance of each individual beam:

$$[C_B] = \sum_{i=1}^{7} \boldsymbol{Tr}\left(C_i', [R_i], \mathbf{t}_i\right) \tag{36}$$

where the compliance matrix $\left[C_i'\right]$, translation vector $\boldsymbol{t}_i$, and rotation matrix $[R_i]$ are listed in Table 1.

Next, we rotate the beams about each of their respective centers by the angle θ and translate their reference frames by $\boldsymbol{d}_j$ to the common reference frame at the center of Hub 2 of the RBL. Following these coordinate transformations, the compliance matrix for each of the four beams can be written as:

$$\left[C_{B,j}(\theta)\right] = \boldsymbol{Tr}\left(\boldsymbol{Tr}(C_B, [R_z(\theta)], \mathbf{0}), I, -\mathbf{d}_j\right), \ j = 1,\ 3 \tag{37}$$

$$\left[C_{B,j}(\theta)\right] = \boldsymbol{Tr}\left(\boldsymbol{Tr}(C_B, [R_z(-\theta)], \mathbf{0}), I, -\mathbf{d}_j\right), \ j = 2,\ 4 \tag{38}$$

where

$$\mathbf{d}_j = \frac{w}{\sqrt{2}}\left[\cos\left(\frac{\pi}{2}j - \frac{\pi}{4}\right), \quad \sin\left(\frac{\pi}{2}j - \frac{\pi}{4}\right), \quad 0\right]^{\mathsf{T}}. \tag{39}$$

Since the four beams are connected in parallel, the stiffness of the entire RBL link can be calculated as the sum of the stiffness matrices of all four beams:

$$[K_{RBL}(\theta)] = \sum_{j=1}^{4} \left[C_{B,j}(\theta)\right]^{-1}. \tag{40}$$

And the compliance matrix of the entire RBL can be obtained by simply inverting the stiffness matrix, i.e.

$$[C_{RBL}(\theta)] = [K_{RBL}(\theta)]^{-1}. \tag{41}$$

Table 2
Properties of the physical prototype .

Total Mass	1.27 kg	Dimensions	408.7 mm × 100 mm × 100 mm
Shaft Diameter (d_1)	4.5 mm	Block Width (w_2)	20 mm
Beam Width (w_3)	25 mm	Beam Thickness (t_3)	0.8 mm
Beam Spacing (h)	65 mm	Beam Length (L_3)	282 mm

Table 3
Numerical values of key parameters used in theoretical modeling.

n	E_n (MPa)	G_n (MPa)	J_n (mm^4)	$I_{x,n}$ (mm^4)	$I_{y,n}$ (mm^4)	L_n (mm)
1	2.00E5	7.6923E4	4.02578E1	2.013E1	2.013E1	8.700
2	6.90E4	2.5940E4	2.2533E4	1.333E4	1.333E4	4.000E1
3	6.90E4	2.5940E4	4.181	1.042E3	1.067	2.820E2

κ_R	1.783E5 N-mm/rad	$k_{x,FG}$	3.880e-2E-2 N/mm
$k_{y,CL}$	1.156 N/mm	$k_{y,FG}$	2.557 N/mm
κ_z	3.841E2 N-mm/rad		

If we define the external load applied to Hub 2 by wrench $\boldsymbol{W}$ and deformation of Hub 2 by twist $\boldsymbol{T}$ as shown in Fig. 5, we have

$$\mathbf{W} = [K_{RBL}(\theta)]\mathbf{T}, \quad \text{or} \quad \mathbf{T} = [C_{RBL}(\theta)]\mathbf{W}, \tag{42}$$

where all matrices and screws are defined in the coordinate frame placed at the center of Hub 2.

4. Discussion of compliance matrices

Now let us discuss the structure of the compliance matrix of the entire RBL $[C_{RBL}(\theta)]$ and its response to the beam rotation angle θ.

When $\theta = 0^\circ$, the compliance matrix has the form:

$$[C_{RBL}(0^\circ)] = \begin{bmatrix} 0 & c_{1,2} & 0 & c_{1,4} & 0 & 0 \\ c_{2,1} & 0 & 0 & 0 & c_{2,5} & 0 \\ 0 & 0 & 0 & 0 & 0 & c_{3,6} \\ c_{4,1} & 0 & 0 & 0 & c_{4,5} & 0 \\ 0 & c_{5,2} & 0 & c_{5,4} & 0 & 0 \\ 0 & 0 & c_{6,3} & 0 & 0 & 0 \end{bmatrix}. \tag{43}$$

Numerical values for all elements can be calculated by substituting all geometric dimensions and material properties from Tables 2 to 3. An exhaustive list of the non-zero matrix components is included in Appendix A. The most important element is perhaps the lateral compliance in the X-axis, $c_{4,1} = 6.4408$ mm/N, or the corresponding stiffness $k_X(0^\circ) = 1/c_{4,1} = 0.15526$ N/mm, which matches exactly with Eq. (25) derived in our previous work [7].

An important behavior of this structure is the buckling it undergoes in lateral loading at beam angles near 90°. A different form of buckling – axial compressive buckling – will be discussed in detail in the next subsection. To consider buckling in our compliance matrices, we simply neglect the stiffness of the buckled beams. For instance, when $\theta = 90^\circ$, the resulting compliance matrix is written as:

$$[C_{RBL}(90^\circ)] = \begin{bmatrix} 0 & c_{1,2} & 0 & c_{1,4} & 0 & 0 \\ c_{2,1} & 0 & c_{2,3} & 0 & c_{2,5} & 0 \\ 0 & c_{3,2} & 0 & 0 & 0 & c_{3,6} \\ c_{4,1} & 0 & c_{4,3} & 0 & c_{4,5} & 0 \\ 0 & c_{5,2} & 0 & c_{5,4} & 0 & c_{5,6} \\ c_{6,1} & 0 & c_{6,3} & 0 & c_{6,5} & 0 \end{bmatrix} \tag{44}$$

Again, numerical values for all elements in $[C_{RBL}(90^\circ)]$ can be calculated by substituting all model parameters as they are listed in Appendix A. Notably, the lateral stiffness for this case is $k_X(90^\circ) = 1/c_{4,1} = 2.3084$ N/mm, which closely matches our previously derived model, Eq. (25). Note this result predicts that the maximum ratio for lateral stiffness is

$$\gamma_{90^\circ} = \frac{k_X(90^\circ)}{k_X(0^\circ)} \approx 14.9. \tag{45}$$

This is the "theoretical maximum stiffness ratio" of the prototype RBL predicted by our analytical model. Later, we will verify the model by comparing this ratio with the experimental test results.

Use of compliance matrices eliminates the need for solving the elementary beam theory equations and makes predictions for multi-axis loading. However, with this technique, it is more difficult to incorporate models of buckling, and it is still a theoretical challenge to merge the matrices produced for each buckled configuration for each type of load. For this reason, when we compare analytical and experimental stiffness as a function of beam angle, we refer back to the simpler analytical models Eqs. (25) and (27). Nevertheless, for designs without significant buckling effects, this compliance matrix modeling approach can be a powerful tool for analyzing variable stiffness links.

5. Axial compressive buckling

The RBL consists of four slender beams that, in the presence of a compressive load in the $-Z$ direction, are susceptible to axial buckling. Accordingly, it would be useful to have a model of the critical force at which this form of buckling occurs in the link. The axial compressive buckling considered in this section is distinct from the buckling resulting from laterally applied loads described in Section 2.1.

The mechanics of the buckling of a beam in compression are described by a fourth-order ordinary differential equation [36]. We assume no external lateral load is present. This ODE is solved by specifying four boundary conditions: two at each end. The critical buckling force of the beam corresponds to the lowest value for the compressive force which gives a non-trivial solution of this ODE. As a result, the critical buckling force is a function of the geometry of the beam, the beam material's elastic modulus, and the type of boundary conditions.

As a link in a serial manipulator arm, the deflection of Hub 2 is unconstrained in either rotation or translation. However, for pure axial loading, the symmetry of the link prevents any rotation of Hub 2 relative to Hub 1. Under these conditions, a simple approximation of the critical buckling force of the link can be constructed by considering just one of the four individual rotating beams and examining the following three cases:

Case 1: Hub 2 of the link translates along the X axis while buckling. This behavior is equivalent to fixed-free (fixed rotation, free translation) buckling boundary conditions in the X or x' axis direction for each of the individual beams within the link. Here, the effective second moment of inertia is a function of the angle of rotation of the beams. For an example of this case, consider $\theta = 0$.

$$P_1^{cr}(\theta) = \frac{\pi^2 E_3 I_{y',3}(\theta)}{L_3^2}, \tag{46}$$

Case 2: Instead of translating along the X or Y axes, Hub 2 can instead stay fixed. In this case, the boundary conditions for the individual beams are fixed-fixed, and the beams will always buckle along their local beam-fixed x axis because $I_{y,3} \ll I_{x,3}$. For this reason, the angle of the beams does not affect the critical buckling force of this case. For an example of this case, consider $\theta = 45^\circ$ or $\theta = -45^\circ$.

$$P_2^{cr} = 4\frac{\pi^2 E_3 I_{y,3}}{L_3^2}, \tag{47}$$

Case 3: The last case is identical to the first except that Hub 2 translates in the Y or y' axis instead, and the effective second moment of area is adjusted accordingly. For an example of this case, consider $\theta = 90^\circ$.

$$P_3^{cr}(\theta) = \frac{\pi^2 E_3 I_{x',3}(\theta)}{L_3^2}. \tag{48}$$

According to Geere [34],

$$I_{y',3}(\theta) = \frac{I_{x,3} + I_{y,3}}{2} - \frac{I_{x,3} - I_{y,3}}{2}\cos(2\theta), \tag{49}$$

and, similarly,

$$I_{x',3}(\theta) = \frac{I_{x,3} + I_{y,3}}{2} + \frac{I_{x,3} - I_{y,3}}{2}\cos(2\theta). \tag{50}$$

These results allow for a simple analytical model of buckling that predicts the occurrence of buckling in the beam sheet by setting the critical buckling force for the link to be the sum of the minimum buckling force of all four beams:

$$P^{cr}(\theta) = 4\min(\{P_1^{cr}(\theta), P_2^{cr}, P_3^{cr}(\theta)\}). \tag{51}$$

Here, the coefficient "4" means that we assume the buckling conditions for all four beams are identical due to the structural symmetry and associated mechanical constraints.

Numerical values for the critical buckling force can be calculated by substituting geometric dimensions and material properties from Tables 2 to 3. The results for the two major angles of interest are: $P^{cr}(0^\circ) \approx 36.5$ N, $P^{cr}(45^\circ) \approx 146.2$ N.

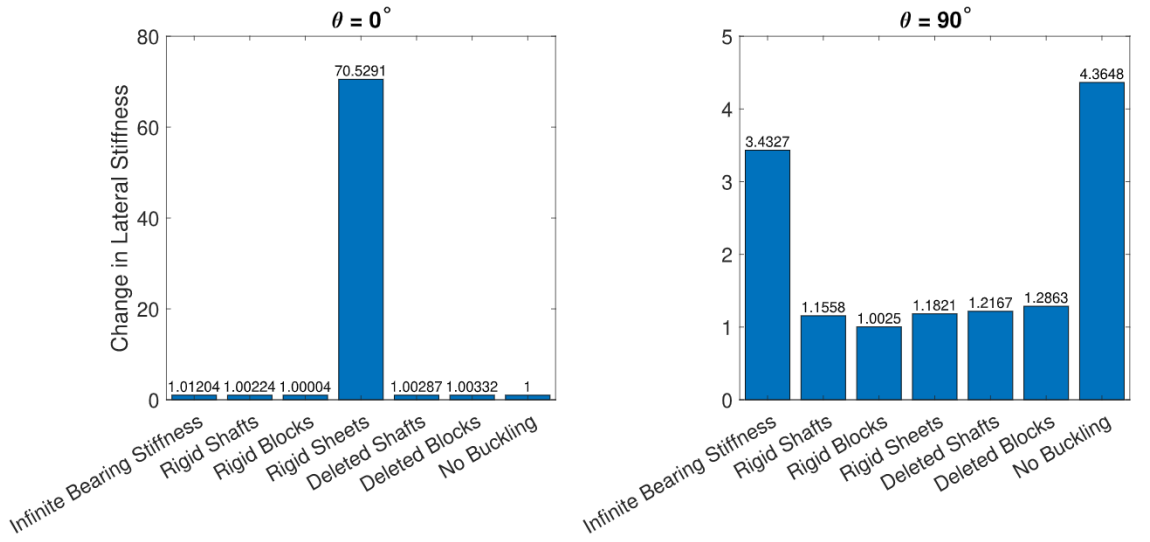

Fig. 6. Visualization of the relative change in lateral stiffness when modifying certain modeling assumptions for both $\theta = 0^\circ$ and $\theta = 90^\circ$. A value of 1 indicates no change. A value of 1.1 indicates a 10% increase in stiffness.

6. Discussion of parasitic compliance

The change in stiffness of the RBL design is intended to come solely from the rotating beam sheets. Their rotating cross-section causes the change in lateral stiffness of the entire link. As a result, it might be tempting to only model their contribution to the compliance of the link. In certain designs, this may be adequate. However, as the beam sheets are rotated into their stiffer configuration, the compliance of the other components of the link – those that are in series with the beam sheets – begin to contribute significantly to the overall compliance. This is a natural consequence of series compliance.

Without taking these other sources of compliance into account, a stiffness model for a VSL can drastically overestimate its stiffness – especially for the stiffer configurations of the mechanism. We call this extra compliance "parasitic compliance" because it reduces the magnitude of the change in stiffness by disproportionately reducing the stiffness of the stiffer configurations of the link, and because the sources of the extra compliance are inherent to the design. This same effect is the reason that additional compliance terms had to be introduced in [1] and [5] to match the analytical models to experimental results.

The three main sources of parasitic compliance in the lateral stiffness model for the RBL are

1. The rotational compliance in the bearings that anchor each end of the shafts to the hubs.
2. The flexibility of the shafts.
3. The flexibility of the blocks that join the sheets to the shafts.

Fig. 6 shows how different assumptions about the rigidity and presence of components of the model change the analytical lateral stiffness. The lateral stiffness in the soft and stiff modes can be calculated by evaluating $1/c_{4,1}$ in Eqs. (43) and (44) based on the properties in Tables 2 and 3. However, in order to demonstrate the effects of certain assumptions on the model, we make certain substitutions. For example, assuming that the bearing stiffness κ_R tends to ∞, barely has any effect on the stiffness in the softer mode ($\theta = 0^\circ$), but increases the stiffness of the stiffer mode ($\theta = 90^\circ$) by a factor of ≈ 3.4. As a result, it is clear that modeling the bearing stiffness is essential to an accurate model of lateral stiffness in this design.

The only beam component that does not have a substantial effect on either the soft mode lateral stiffness or the stiffer mode lateral stiffness is the block. At most, assuming the blocks are inflexible increases the stiffness of the model by a factor of 1.0025. However, the length of the blocks is not as negligible. Taking the limit as L_2 tends to 0 gives the result in Fig. 6 labeled "Deleted Blocks" which shows a corresponding increase in stiffness by a factor of 1.29. As a result, it is clear that even if the rigidity of the block segments is negligible, their geometry is not.

There is one other source that could arguably be considered parasitic compliance: the buckling effect. Because the buckling of the back beams under lateral loads changes the boundary conditions of the front, unbuckled beams from fixed-guided to cantilever, it has a drastic effect on their stiffness. According to Fig. 6, assuming the "No Buckling" condition increases stiffness by a factor of 4.36.

Therefore, based on Fig. 6, one could conclude that the most important components to model are, in order:

1. the beam sheets.
2. the buckling effect.
3. the bearing stiffness.

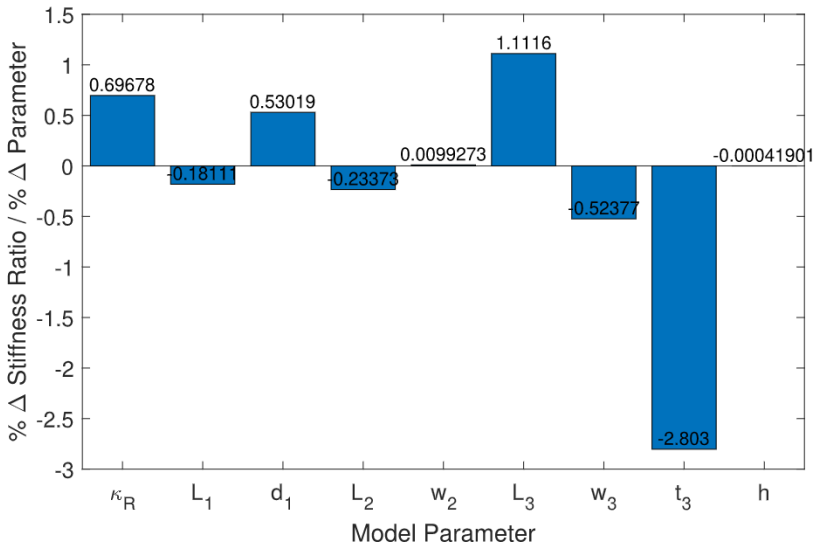

Fig. 7. The linearized change in stiffness ratio by change in parameter.

4. the blocks.
5. the shafts.

One final conclusion we can draw from this figure is that modeling stiffness of the VSL is simpler in its softer configuration. Under these conditions, the strain is more concentrated in the compliant sheets, and so only their compliance needs to be considered. However, modeling is significantly more complex for the stiffer mode. In this mode the strain is distributed throughout a variety of components with similar compliance contributions – failing to adequately consider any one of them could significantly invalidate a model. Thus, future designers of VSLs should give strong consideration to minimizing their design's sources of parasitic compliance when designing a VSL to meet a certain stiffness goal and to accurately modeling their design's sources of parasitic compliance when modeling the result.

7. Parameter sensitivity analysis

In Fig. 7, we compute the gradient of the stiffness ratio with respect to the parameters in the model that define the design, and normalize them with respect to their current values to get the gradient components in terms of percent change, we can compare them to get a sense of the best way to alter the design to optimize the stiffness ratio. Decreasing the beam sheet thickness is predicted to give the largest effect on stiffness ratio. By comparison, changing the beam spacing h, or the block width w_2 are predicted to have very little effect. Another good candidate for increasing the stiffness ratio is increasing the beam sheet length L_3.

However, the stiffness ratio should not be increased blindly. If both the maximum and minimum stiffness decrease proportionally, as the minimum stiffness tends toward zero, the ratio will of course tend toward infinity. We have increased the stiffness ratio, but only by decreasing the average stiffness of the structure. In most cases, this is undesirable.

More commonly, we want to specify a maximum stiffness for the soft mode or a minimum stiffness for the stiff mode, and optimize the stiffness ratio thereafter. In this case, we can divide the parameters in Fig. 7 into two groups. First, there are the parameters associated with parasitic compliance $(\kappa_R, L_1, d_1, L_2, w_2)$. The goal for these parameters should always be to minimize their associated compliance. This means reducing their length, maximizing their rigidity, and so on. Second, there are the parameters associated with the beam sheets – the components that are intended to be used to achieve the variable stiffness effect.

In general, we can be sure that increasing the stiffness of the parasitic compliant components will increase the stiffness ratio without decreasing the soft mode stiffness. In this regard, decreasing the shaft diameter has a large effect on the ratio as does increasing the bearing stiffness κ_R.

Fig. 8 indicates the effect that the beam sheet parameters have on the soft mode stiffness, the stiff mode stiffness, and the overall stiffness ratio assuming the parasitic compliance is unchanged. The contours indicate that increasing L_3 or decreasing t_3 increase the stiffness ratio, but only by decreasing both the soft mode stiffness and the stiff mode stiffness. The aspect ratio of the beams w_3/t_3 is actually near optimal for the thickness, length, and parasitic compliance of the design given that it is near the point where both increasing and decreasing it result in a decrease in the stiffness ratio.

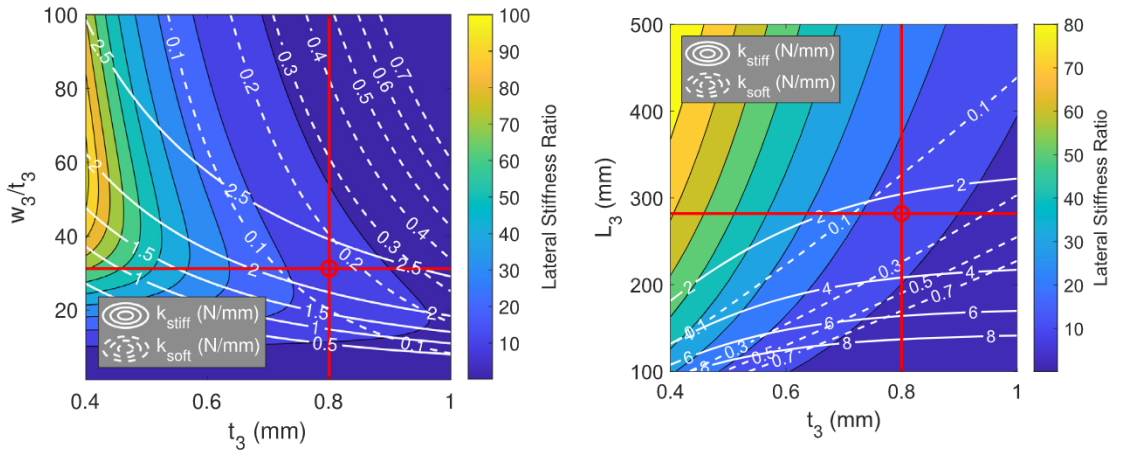

Fig. 8. Contour maps of the effect of changing the beam sheet thickness t_3, the beam sheet aspect ratio w_3/t_3, and the beam sheet length on the lateral stiffness. The filled contours show the lateral stiffness ratio. The solid and dashed contour lines show the stiff mode stiffness ($\theta = 90°$) and the soft mode stiffness ($\theta = 0°$). The red lines indicate the properties of the prototype design. (For interpretation of the references to colour in this figure, the reader is referred to the web version of this article.)

Table 4
FEA Model Fit Parameters – Torsional Stiffness and Axial Buckling.

Parameter	Value	Unit
k_1	0.2071	N/mm
k_2	2.498	N/mm
A	106.09	N
B	9.008	–
C	128.43	°
D	158.88	N
F	148.79	N

8. Finite element analysis

A finite element model of the RBL was constructed in ABAQUS to collect simulation data for comparison with both analytical and experimental results. The components were simplified into representative geometry. The beam sheets were modeled with 2D shell elements, while the rest of the beam components were modeled with solid elements. Because the RBL design involves long slender beams, buckling must be considered in the simulation. To take buckling into account, simulation of the link was accomplished in three steps:

Step 1: An eigenvalue buckling analysis was conducted for the load in question to identify buckling modes and their associated mode shapes.
Step 2: The nodal deflections associated with those buckling mode shapes were scaled such that the maximum deflection matched a certain imperfection size and then seeded into the model.
Step 3: A non-linear Riks-method static analysis was run with the desired load.

Stiffness was extracted by measuring the slope of the first few points of the load vs. deflection curve. Critical buckling forces were extracted directly from the eigenvalue buckling analysis.

The torsional stiffness of the FEA model of the link is best fit ($R^2 = 0.9990$) by the following expression:

$$\kappa_Z(\theta) = h^2((k_1 + k_2) - (k_1 - k_2)\sin(2\theta)) \tag{52}$$

The critical axial buckling force of the FEA model of the link is best fit ($R^2 = 0.9987$) by the following expression on the interval $\theta \in [0°, 45°]$ and is otherwise a periodic even function with a period of 90°.

$$P^{cr}(\theta) = \min(A\arctan(B\theta + C) + D, F), \ \theta \in [0°, 45°] \tag{53}$$

The numerical values of parameters for both of these functions are listed in Table 4.

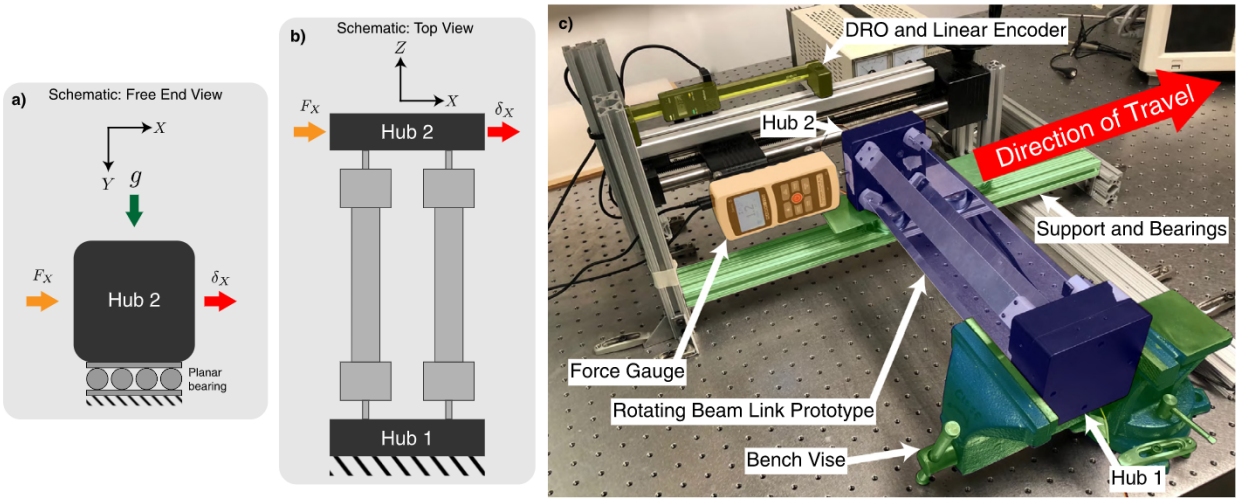

Fig. 9. The experimental setup used to test the lateral stiffness of the link. Deflection is measured via a linear encoder. The force is measured with a force gauge. Hub 1 is fully clamped with a bench vise and Hub 2 is supported in the vertical direction by bearings which allow movement in the horizontal plane so as not to restrict lateral movement or shortening of the link.

9. Experimental results

In this section, we detail experiments conducted to verify our models of stiffness and buckling determined in previous sections and discuss the results. In addition, we provide data on the power required to actuate the rotating beams of the link while subjected to a lateral displacement load.

9.1. Experimental apparatus

Force and deflection data were collected while the link was loaded in several different ways. Fig. 9 illustrates, for example, the setup used to test the lateral stiffness of the link. In each experiment, deflection data was collected with a linear encoder/DRO,[1] and the reaction force was collected with a force gauge.[2] Both sensors were mounted on a manually-driven test stand[3] which was actuated quasi-statically. In each experiment, the link lay horizontally with Hub 1 fixed to ground. When measuring lateral force or axial buckling force, Hub 2 was supported by ball roller bearings which allowed it to move freely in the horizontal plane. When measuring torsion, the force gauge was instead connected to a cable that was fixed to a pulley so as to produce a torque. The pulley was fixed to a shaft that was mated to Hub 2. Care was taken to arrange the bearings supporting the shaft such that the transverse load from the cable was isolated from the link and only a torque around the central axis of the link was transmitted.

9.2. Measured stiffness

The stiffness ratio of the prototype is the ratio between its maximum and minimum lateral stiffness. As experimentally determined, the lateral stiffness in the X direction for the beam angle $\theta = 90^\circ$ was $k_X^*(90^\circ) = 2.245$ N/mm and the minimum stiffness at a beam angle of 0° was $k_X^*(0^\circ) = 0.1613$ N/mm. The ratio of the maximum experimental lateral stiffness over the minimum experimental lateral stiffness gives the prototype stiffness ratio:

$$\gamma_{90^\circ}^* = \frac{k_X^*(90^\circ)}{k_X^*(0^\circ)} \approx 13.9\,. \tag{54}$$

Fig. 10a) depicts a comparison of all of the experimental results and analytical models presented in this paper, with Fig. 10b) included for reference. Lateral stiffness and torsional stiffness are both described with sinusoids of the same period. Notably, however, they are offset by 45°. The lateral stiffness model is a close match to the experimental results. The experimental torsional stiffness results are not as well matched by the analytical model. In this case, the torsional stiffness under-performs the expectations of the analytical Eq. (27) and FEA models Eq. (52). This discrepancy is most likely due to compliance induced by imperfections and clearances at the interfaces between different sections of the beam combined with complex buckling of the beam sheet and compliance introduced by the measurement apparatus itself. The stiffer regimes

[1] Mitutoyo ABSOLUTE Digimatic SD-/6″D. Resolution: 0.01 mm.
[2] MARK-10 M5-100. Resolution: 1 N.
[3] MARK-10 ES30.

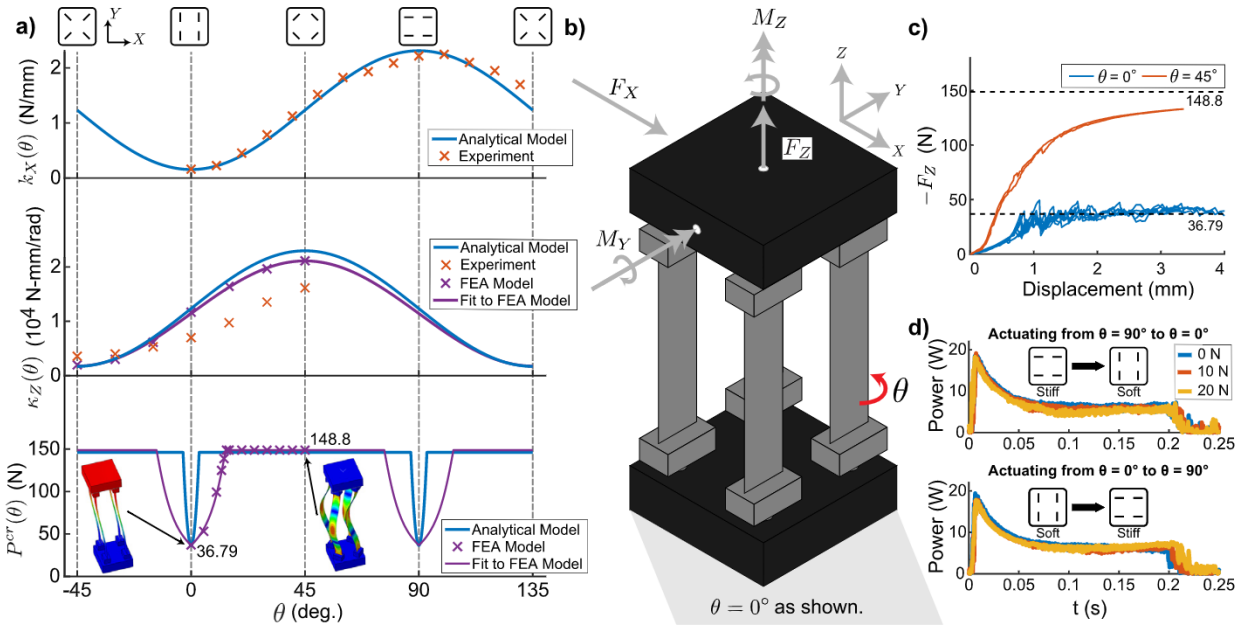

Fig. 10. An overview of the results of experiments on the prototype. a) Comparison of experimental results, FEA models, and analytical models of the lateral stiffness, k_X, which relates F_X to δ_X; torsional stiffness, κ_Z, which relates M_Z to ϕ_Z; and critical axial buckling force, P^{cr}. b) A schematic of the design for reference. c) Depiction of load vs displacement results for axially compressive loads related to buckling. References are provided to loads predicted by the FEA model. 148.8 N corresponds to the peak critical buckling force. 36.79 N corresponds to the buckling forces predicted by the FEA model at 0°. d) Comparison of power requirements when actuating between the stiffest and softest lateral stiffness modes while under a constant lateral deflection load. The prototype was loaded to a target load (e.g. 20 N) in its stiff mode ($\theta = 90°$) and then actuated to the soft mode ($\theta = 0°$) and back while measuring servo power draw.

of torsional stiffness are at the limits of what we can accurately measure with the available apparatus. As a result, it is not surprising that the stiffer torsional results are lower than the analytical and FEA modeling predictions. Modeling the causes of this behavior may be challenging, but for the purposes of control, a model can always be determined empirically from this data.

9.3. Buckling

The FEA results described in Eq. (53) also under-perform the analytical model of buckling in Eq. (51). The FEA indicates the beams buckling in the fixed-free condition at angles up to 15° compared to the approximately 3° predicted by the analytical model. However, the most important states to consider for buckling are the cases at the critical angles of maximum or minimum lateral or torsional stiffness: 0°, 45°, and 90° which are approximately 37 N, 149 N, and 37 N which is confirmed by an approximate consensus of the analytical model, FEA model, and experimental results. Fig. 10c) shows experimental force vs. deflection results for axial compressive buckling of the RBL with the critical buckling forces compared to the load curves at two critical angles. The case for 0° clearly shows the link in a buckled state – unable to support load beyond the critical force. The case for 45° shows the load asymptotically approaching a value near the critical buckling force predicted by the models.

In theory, one can obtain an analytical model of buckling that is more accurate to the FEA results by using a piecewise domain that incorporates the torsion springs, shafts etc. combined with a compound buckling model that allows for bending in two dimensions. However, the complexity of such a model precludes the existence of a tractable closed-form solution and the gains in accuracy provided by such a model are marginal. In general, deriving an analytical model that accurately matches FEA and experimental behavior for small beam rotation angles remains an unsolved problem in elastic stability theory.

10. Conclusions

The rotating beam link (RBL) variable stiffness link (VSL) design can be modeled via both planar and spatial methods. The planar method presented here has the advantage of a clear closed form solution as a function of the beam angle θ but requires solving the piecewise classical Euler-Bernoulli beam in order to include all the sources of compliance. The spatial method avoids this step but cannot be expressed as a closed-form function of θ if buckling has to be modeled by simulating removing beams. For other mechanisms where buckling effects do not need to be accounted for, the spatial derivation is more straightforward and makes predictions about multiple modes of stiffness (torsional, lateral, axial, etc.) simultaneously.

An additional challenge of modeling this link design is accurately modeling axial buckling. As the beams rotate by θ, the mode of buckling changes. For values of θ near 0, the link tends to buckle in a fixed-free mode. Otherwise, the symmetric design enforces an intrinsic fixed-fixed constraint form of buckling and the critical buckling force is not a function of θ. By calculating the critical buckling force associated with both of these conditions and using the minimum, a simple piecewise function provides a good approximation of the actual behaviour for critical angles of interest. For a more accurate model of buckling for small beam angles, additional novel theoretical work may be required.

Developing analytical models of the RBL design provides useful insight into design improvement recommendations. For example, it illuminates the problem of the parasitic compliance effect: the increase in compliance associated with the components required to actuate the variable stiffness device. For the RBL design, these sources include the length and elasticity of the shafts and blocks that mount the beams. Additionally, the slight rotational compliance of the bearing that fixes the shafts makes a significant contribution to the parasitic compliance effect. The parasitic compliance effect is also observed in other desings of other VSL concepts. Subsequent VSL designs should focus on minimizing this parasitic compliance effect by designing ancillary components to be sufficiently rigid. For the RBL design, this would involve increasing shaft diameter, decreasing the length of the shafts and blocks, and minimizing the bearing compliance.

Declaration of Competing Interest

The authors declare that they have no known competing financial interests or personal relationships that could have appeared to influence the work reported in this paper.

Appendix A. Compliance matrix components

The following tables contain the numerical values of components of the compliance matrix as derived in the text (Tables A.1 and A.2).

Table A.1
Components of the compliance matrix $[C_{RBL}(0^\circ)]$ in Eq. (43).

Component $c_{i,j}$	Value	Unit
$c_{1,2}$, $c_{5,4}$	-8.0693×10^{-6}	1/N
$c_{1,4}$	4.8801×10^{-8}	1/(N-mm)
$c_{2,1}$, $c_{4,5}$	8.1607×10^{-6}	1/N
$c_{2,5}$	4.9354×10^{-8}	1/(N-mm)
$c_{3,6}$	8.0181×10^{-5}	1/(N-mm)
$c_{4,1}$	6.4408	mm/N
$c_{5,2}$	9.9400×10^{-2}	mm/N
$c_{6,3}$	5.2133×10^{-5}	mm/N

Table A.2
Components of the compliance matrix $[C_{RBL}(90^\circ)]$ in Eq. (44).

Component $c_{i,j}$	Value	Unit
$c_{1,2}$, $c_{5,4}$	-1.6321×10^{-5}	1/N
$c_{1,4}$	9.8708×10^{-8}	1/(N-mm)
$c_{2,1}$, $c_{4,5}$	1.4338×10^{-3}	1/N
$c_{2,3}$, $c_{6,5}$	-2.8182×10^{-4}	1/N
$c_{2,5}$	8.6713×10^{-6}	1/(N-mm)
$c_{3,2}$, $c_{5,6}$	-5.2812×10^{-3}	1/N
$c_{3,6}$	1.6250×10^{-4}	1/(N-mm)
$c_{4,1}$	0.4332	mm/N
$c_{4,3}$, $c_{6,1}$	-4.6598×10^{-2}	mm/N
$c_{5,2}$	13.0532	mm/N
$c_{6,3}$	9.2633×10^{-3}	mm/N

References

[1] Y. She, H.-J. Su, D. Meng, C. Lai, Design and modeling of a continuously tunable stiffness arm for safe physical human robot interaction, J. Mech. Rob. 12 (1) (2020), doi:10.1115/1.4044840.
[2] A. Stilli, H.A. Wurdemann, K. Althoefer, A novel concept for safe, stiffness-controllable robot links, Soft Rob. 4 (1) (2017) 16–22, doi:10.1089/soro.2016.0015.
[3] R. Hu, V. Venkiteswaran, H.-J. Su, A variable stiffness robotic arm design using linear actuated compliant parallel guided mechanism, in: IFToMM Symposium on Mechanism Design for Robotics, Springer, Cham, 2017, p. 62, doi:10.1007/978-3-030-00365-4_5.
[4] Y. She, H.-J. Su, D. Meng, S. Song, J. Wang, Design and modeling of a compliant link for inherently safe corobots, J. Mech. Rob. 10 (1) (2018) 011001, doi:10.1115/1.4038530.
[5] V.K. Venkiteswaran, R. Hu, H. Su, A pneumatically-actuated variable-stiffness robot arm using parallel flexures, in: 2018 IEEE International Conference on Robotics and Biomimetics (ROBIO), IEEE, 2018, pp. 1–7, doi:10.1109/ROBIO.2018.8665208.
[6] T. Wang, J. Zhang, Y. Li, J. Hong, M.Y. Wang, Electrostatic layer jamming variable stiffness for soft robotics, IEEE/ASME Trans. Mechatron. 24 (2) (2019) 424–433, doi:10.1109/TMECH.2019.2893480.
[7] T. Morrison, C. Li, X. Pei, H.-j. Su, A novel rotating beam link for variable stiffness robotic arms, in: 2019 IEEE International Conference on Robotics and Automation (ICRA), Montreal, QC, Canada, 2019, pp. 9387–9393.
[8] Y. She, D. Meng, J. Cui, H.J. Su, On the impact force of human-robot interaction: joint compliance vs. link compliance, in: 2017 IEEE International Conference on Robotics and Automation (ICRA), Singapore, 2017, pp. 6718–6723, doi:10.1109/ICRA.2017.7989795.
[9] J. López-Martínez, D. García-Vallejo, J.L. Torres, A. Giménez, J.A. López, Role of link flexibility and variable stiffness actuator on collision safety for service robots, in: Mechanisms and Machine Science, vol. 7, Springer, 2013, pp. 499–507, doi:10.1007/978-94-007-4902-3_53.
[10] S. Song, X. Zeng, Y. She, J. Wang, H.J. Su, Modeling and control of inherently safe robots with variable stiffness links, Rob. Auton. Syst. 120 (2019) 103247, doi:10.1016/j.robot.2019.07.017.
[11] Y. She, S. Song, H.-J. Su, J. Wang, A comparative study on the effect of mechanical compliance for a safe physical human robot interaction, J. Mech. Des. 142 (6) (2020), doi:10.1115/1.4046068.
[12] L. Blanc, A. Delchambre, P. Lambert, Flexible medical devices: review of controllable stiffness solutions, Actuators 6 (3) (2017) 23, doi:10.3390/act6030023.
[13] L.L. Howell, A. Midha, T.W. Norton, Evaluation of equivalent spring stiffness for use in a pseudo-rigid-body model of large-deflection compliant mechanisms, J. Mech. Des. 118 (1) (1996) 126–131, doi:10.1115/1.2826843.
[14] L.L. Howell, Compliant Mechanisms, Wiley-Interscience, 2001.
[15] Y. She, D. Meng, H.J. Su, S. Song, J. Wang, Introducing mass parameters to pseudo rigid body models for precisely predicting dynamics of compliant mechanisms, Mech. Mach. Theory 126 (2018) 273–294, doi:10.1016/j.mechmachtheory.2018.04.005.
[16] S. Awtar, S. Sen, A generalized constraint model for two-dimensional beam flexures: nonlinear load-displacement formulation, J. Mech. Des. 132 (8) (2010) 0810081–08100811, doi:10.1115/1.4002005.
[17] F. Ma, G. Chen, Modeling large planar deflections of flexible beams in compliant mechanisms using chained beam-constraint-model, J. Mech. Rob. 8 (2) (2016), doi:10.1115/1.4031028.
[18] G. Chen, F. Ma, G. Hao, W. Zhu, Modeling large deflections of initially curved beams in compliant mechanisms using chained beam constraint model, J. Mech. Rob. 11 (1) (2019), doi:10.1115/1.4041585.
[19] G. Chen, R. Bai, Modeling large spatial deflections of slender bisymmetric beams in compliant mechanisms using chained spatial-beam constraint model, J. Mech. Rob. 8 (4) (2016), doi:10.1115/1.4032632.
[20] R.P. Chase, R.H. Todd, L.L. Howell, S.P. Magleby, A 3-D chain algorithm with pseudo-rigid-body model elements, Mech. Based Des. Struct. Mach. 39 (1) (2011) 142–156, doi:10.1080/15397734.2011.541783.
[21] H.-J. Su, D.V. Dorozhkin, J.M. Vance, A screw theory approach for the conceptual design of flexible joints for compliant mechanisms, J. Mech. Rob. 1 (2009) 41009, doi:10.1115/1.3211024.
[22] H.-J. Su, H. Shi, J. Yu, A symbolic formulation for analytical compliance analysis and synthesis of flexure mechanisms, J. Mech. Des. 134 (5) (2012) 051009, doi:10.1115/1.4006441.
[23] P. Qi, C. Qiu, H. Liu, J.S. Dai, L.D. Seneviratne, K. Althoefer, A novel continuum manipulator design using serially connected double-layer planar springs, IEEE/ASME Trans. Mechatron. 21 (3) (2016) 1281–1292, doi:10.1109/TMECH.2015.2498738.
[24] H. Li, G. Hao, Constraint-force-based approach of modelling compliant mechanisms: principle and application, Precis. Eng. 47 (2017) 158–181, doi:10.1016/j.precisioneng.2016.08.001.
[25] S. Huang, J.M. Schimmels, Synthesis of point planar elastic behaviors using three-joint serial mechanisms of specified construction, J. Mech. Rob. 9 (1) (2017), doi:10.1115/1.4035189.
[26] J.J. Rice, J.M. Schimmels, Passive compliance control of redundant serial manipulators, J. Mech. Rob. 10 (4) (2018), doi:10.1115/1.4039591.
[27] A. Bicchi, M.A. Peshkin, J.E. Colgate, Safety for physical human robot interaction, in: Springer Handbook of Robotics, Springer Berlin Heidelberg, Berlin, Heidelberg, 2008, pp. 1335–1348, doi:10.1007/978-3-540-30301-5_58.
[28] S. Song, J. Wang, Y. She, H. Su, Barrier Lyapunov function based control of a flexible link co-robot with safety constraints, in: ASME 2018 Dynamic Systems and Control Conference, DSCC 2018, vol. 3, American Society of Mechanical Engineers (ASME), 2018, doi:10.1115/DSCC2018-9006.
[29] S. Song, Y. She, J. Wang, H.-J. Su, Toward tradeoff between impact force reduction and maximum safe speed: dynamic parameter optimization of variable stiffness robots, J. Mech. Rob. 12 (5) (2020), doi:10.1115/1.4046839.
[30] S. Haddadin, A. De Luca, A. Albu-Schäffer, Robot collisions: a survey on detection, isolation, and identification, IEEE Trans. Rob. 33 (6) (2017) 1292–1312, doi:10.1109/TRO.2017.2723903.
[31] F. Flacco, T. Kröger, A. De Luca, O. Khatib, A depth space approach to human-robot collision avoidance, in: 2012 IEEE International Conference on Robotics and Automation, IEEE, Saint Paul, MN, 2012, pp. 338–345, doi:10.1109/ICRA.2012.6225245.
[32] M. Manti, V. Cacucciolo, M. Cianchetti, Stiffening in soft robotics: a review of the state of the art, IEEE Rob. Autom. Mag. 23 (3) (2016) 93–106, doi:10.1109/MRA.2016.2582718.
[33] Y. She, H.-J. Su, C. Lai, D. Meng, Design and prototype of a tunable stiffness arm for safe human-robot interaction, in: ASME 2016 International Design Engineering Technical Conferences and Computers and Information in Engineering Conference, American Society of Mechanical Engineers, Charlotte, NC, 2016, doi:10.1115/DETC2016-59523. V05BT07A063V05BT07A063
[34] J.M. Geere, Mechanics of Materials, Thomas Learning, 2004.
[35] W.C. Young, R.G. Budynas, A.M. Sadegh, Roark's Formulas for Stress and Strain, third ed., McGraw-Hill Education, New York, NY, USA, 2012.
[36] S.P. Timoshenko, J.M. Gere, Theory of Elastic Stability, second ed., Dover Publications, 2009.